*Clays and Clay Minerals* (2025), **73**, e23, 1–12
doi:10.1017/cmn.2025.8

**Original Paper**

# Influence of force field on clay–water contact angle determination using molecular dynamics

L. Guérin[1], T. Bernhard[1], L. Michot[1], E. Ferrage[2], F. Claret[3] and V. Marry[1]

[1]Sorbonne University, Laboratoire PHENIX UMR CNRS 8234, 4 place Jussieu, case 51, 75005 Paris, France; [2]IC2MP, Equipe HydrASA, UMR 7285 CNRS/Université de Poitiers, 86073 Poitiers, France and [3]BRGM, 3 avenue claude Guillemin, BP 36009 - 45060 Orléans Cedex 2, France

## Abstract

Clay minerals wettability is a key property for predicting water distribution and pollutant migration in natural or artificial materials. This study attempted to understand the difference in hydrophilicity due to the exchange of structural hydroxyl groups by fluorine atoms, observed in a number of clays. To this end, contact angles of water droplets on hydroxylated and fluorinated talcs were calculated from molecular simulations with two different force fields (one non-polarizable and one polarizable). In parallel, careful measurements of contact angles on a hydroxylated talc monocrystal were undertaken in order to assess the ability of the force fields to reproduce experiments. As expected, fluorinated talc was slightly more hydrophobic than hydroxylated talc for both force fields. Moreover, although the two force fields lead to fluid properties at the interface that were significantly different, the associated contact angles (and related works of adhesion) remained quite close to each other and to contact angles obtained on similar silica-type surfaces. These contact angles overestimated the experimental ones. This could be tentatively assigned to the presence of steps on monocrystal surfaces that could slightly increase the hydrophilicity of the surface, resulting in slightly lower contact angles. When analyzing more carefully the differences between both force fields, it appeared that the use of a polarizable force field resulted in a higher depletion of the fluid close to the surface. This could indicate less attraction between the fluid and the solid and a lesser constraint for the fluid. The combination of these two effects leads to a lower entropy loss and consequently to slightly higher work of adhesion.

**Keywords:** contact angle; fluorinated talc; hydrophobicity; molecular dynamic; talc; work of adhesion

(Received: 07 November 2024; revised: 12 February 2025; accepted: 28 February 2025)

## Introduction

Clays are lamellar minerals commonly found in rocks, soils, or sediments. Their minute particle sizes and associated large surface area control to a significant extent the fate of a wide range of inorganic or organic pollutants in rocks, soils, or sediments (Yang et al., 2022; Ye et al., 2022). In addition, the surface properties of clays are also beginning to be used as barriers against the spread of contaminants in the context of nuclear waste repositories (Charlet et al., 2017; Landais, 2006). However, in many situations, these clay-rich porous media are only partially water-saturated and pollutant mobility is then controlled by the short-range surface wettability that in turn governs: (1) the distribution of water in the pore network; (2) the connectivity for solute migration (Gimmi and Churakov, 2019; Wang et al., 2022; Yang et al., 2024). For these reasons, understanding the wettability of clay minerals is a key parameter for establishing comprehensive predictions of water distribution and pollutant migration in natural or artificial materials. In that regard, contact angle is an important physical dimension. Contact-angle measurements are often used to characterize clay–water interaction and evaluate the amount and distribution of water in the pore network for a given relative humidity, through the application of the Young-Laplace equation (Gimmi and Churakov, 2019)). However, little is known about the variability in contact angles to be used in such models. This can be particularly detrimental in the case of clayey materials, considering the wide compositional variability of clay minerals that is well illustrated by the family of 2:1 clay minerals. The crystal structure of these materials is based on two opposing tetrahedral sheets sandwiching a central octahedral sheet (Brigatti et al., 2006). This 2:1 layer can be neutral (e.g. talc, pyrophyllite) or negatively charged when chemical isomorphic substitutions in both the tetrahedral or octahedral sheets induce a permanent layer-charge deficit, compensated by cations located in the interlayer space (e.g., smectite, vermiculite, micas). The amount of charge and nature of cation are well known to govern clay–water interactions (Ferrage, 2016; Hendricks et al., 1940; Méring, 1946; Sato et al., 1992) and can then also affect wettability (Szczerba et al., 2020). For this reason, contact-angle measurements of various clay minerals have been performed in the literature generally by macroscopic experiments where a water drop is deposited on the surface of monocrystals, when available, or on pressed clay powders. The visual inspection of the shape of the droplet then allows determination of the contact angle. Whereas all experiments showed that neutral clays such as talc are far

**Corresponding author:** V. Marry; Email: virginie.marry@sorbonne-universite.fr
**Cite this article:** Guérin L., Bernhard T., Michot L., Ferrage E., Claret F., & Marry V. (2025). Influence of force field on clay–water contact angle determination using molecular dynamics. *Clays and Clay Minerals* **73**, e23, 1–12. https://doi.org/10.1017/cmn.2025.8

© The Author(s), 2025. Published by Cambridge University Press on behalf of The Clay Minerals Society.

more hydrophobic than charged ones, results for charged samples displayed a strong variability that did not allow derivation of clear answers on the influence of the crystal chemistry of clay minerals on their wettability. One reason for such dispersion lies in the common use of compacted powders (as monocrystals are scarce) for which particle size, orientation, and porosity all affect wettability. One possible way of overcoming this drawback is to use molecular simulations in which the clay–water interface is well defined. In addition, molecular simulations provide information about the thermodynamic properties of the fluids close to the solid surfaces (Rotenberg et al., 2011). Still, to be relevant, molecular simulations must concur with experimental results and it has been shown repeatedly that the choice of inter-atomic force field used in the simulation is crucial. As far as clays are concerned, several classical force fields have been developed (Cygan et al., 2004; Heinz et al., 2005; Pitman and van Duin, 2012; Skipper et al., 1989; Zhang et al., 2024). The very popular Clay Force Field *ClayFF* (Cygan et al., 2004) has been shown to be very efficient at investigating clay–water interactions, Still, the detailed analysis revealed certain limitations in the description of hydration states and transport properties (Marry et al. 2008, 2011, 2013, 2024), in particular of fluorinated clays, and more generally of the interface between clay and water (Ferrage et al., 2011; Hånde et al., 2018; Tesson et al., 2018). To circumvent this drawback, it could be relevant to include the polarizability of atoms (Daub et al., 2018: Kamath et al., 2013; Le Crom et al., 2020; Wick and Cummings, 2011) and some researchers have been active in the development of a polarizable force field for clay/water/ion systems, referred to as *PIM* (Polarizable Ion Model), specifically adjusted to reproduce ab initio calculation results. Over several years, this force field has yielded promising results regarding the structure, thermodynamics, and diffusion of ion/water systems (Tazi et al., 2012). It has also shown good agreement with experimental results for the structure of clays and the properties of water and ions in the interlayer space (Le Crom et al., 2020; Tesson et al., 2016, 2017, 2018). In the present study, the potential of molecular simulations to describe clay wettability was explored by focusing on a neutral 2:1 clay mineral, i.e. talc. The emphasis was on the influence of crystal chemistry with analysis in parallel of the wettability of a hydroxylated talc sample and a fluorinated one in which structural hydroxyls were replaced by fluorine atoms. Such a substitution has been shown to modify the amount of water interacting with the structure, fluorinated clays accommodating less water than their hydroxylated counterparts for the same relative humidity (Dazas et al., 2013; Malikova et al., 2007; Michot et al., 1994). Two force fields were used, i.e. *ClayFF* and *PIM* and their ability to reproduce experimental contact angles measured on a hydroxylated talc monocrystal was assessed. After deriving *PIM* parameters for fluorine, this then allowed us to perform molecular simulations on fluorinated talc to extend our understanding of the role played by fluorine on clay wettability and on the thermodynamic properties of the fluid at the clay–water interface.

## Materials and methods

### *Experimental procedure*

The talc sample was obtained from the Trimouns deposit located in the French Pyrénées, about 100 km south of Toulouse (France), at an altitude of 1700 m. The sample consisted of centimetric flakes, a quality that is commonly referred to as "talc flower" (Ferrage et al., 2006). The chemical composition was close to that of the $Mg_3Si_4O_{10}(OH)_2$ hydrogenated end-member but with minor amounts of Fe, Al, and F, and traces of Mn, Ti, Cr, Ni, Na, and K (Martin et al., 1999). In this sample, clay layers were all stacked in the same direction. Consequently, detrimental effects linked to the presence of grain boundaries in powder samples, i.e. roughness, sample swelling, and liquid penetration that affect contact angle measurements were reduced significantly. Still, the sample contained steps with depths reaching 100 nm (Ferrage et al., 2006), which decreased the measured contact-angle values compared to a pristine and ideally flat surface. Moreover, the contact-angle value varied depending on where the drop was placed on the surface. To obtain an accurate measurement, it was then necessary to measure a large number of drops at different locations on the sample. Unfortunately, fluorinated talc is not available in single-crystal form, and no contact-angle measurement values are listed in the literature.

Water contact-angle measurements on talc monocrystals were carried out using the static sessile drop method using a drop analyser DSA30 from Krüss GmbH, Hamburg, Germany. Contact-angle values were obtained by depositing a 5 µL of ultra-pure water drop dispensed by a 500 µL syringe attached to a 0.5 mm diameter steel needle. Prior to water–drop deposition, the talc samples were cleaved using scotch tape seconds before the measurement. In order to avoid sample deformation and breaking, a rigid carbon double-sided tape was used.

The circle fitting method was used to calculate contact angles. The drop contour was fitted to a circle segment, and the contact angle was measured at the point where this segment intersected the baseline. A representation of an experimental drop is shown Fig. 1.

Experimentally, the baseline is a line drawn tangentially to the solid surface at the point where the liquid droplet meets the solid surface. It is used as a reference line for measuring the contact angle. If the baseline is drawn too high or too low, it can cause the apparent contact angle to be larger or smaller than its actual value. In the present study, the description of the baseline was difficult, partially due to the roughness of the sample resulting from the partial peeling of bits of the monocrystal. The procedure was as follows: for each drop, the angle was measured for the two extreme positions of the base line, depicted in Fig. 1. These two

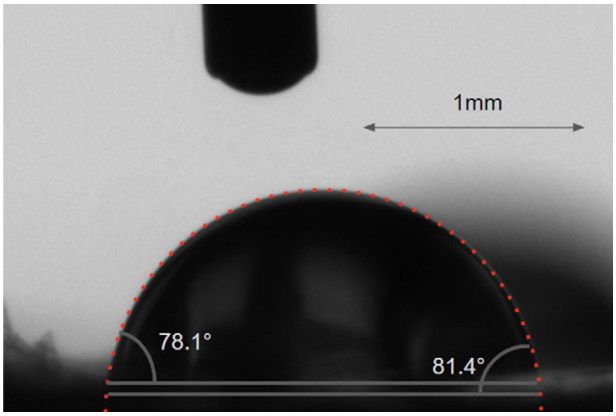



**Figure 1.** Representation of the circle method and the influence of the baseline placement on the measured contact angle.

https://doi.org/10.1017/cmn.2025.8 Published online by Cambridge University Press

extreme baselines were separated by 0.07 mm, which corresponds to about 7% of the drop radius. The contact angle for the drop was determined by taking the mean of the two resulting angles.

## Molecular simulations

### *Description and parametrization of the* PIM

As explained in previous studies (Hånde et al., 2018; Le Crom et al., 2020; Tesson et al., 2016, 2017, 2018), the use of the *PIM* force field was justified by the improvements it can bring due to the inclusion of polarizability in the interactions at the clay–fluid interface. However, as the *PIM* parameters for fluorine have not been determined previously, the following paragraphs present the development of the force field for fluorinated clays.

The *PIM* potential is composed of the following terms:

$$V_{\text{Total}} = V_{\text{Charge}} + V_{\text{Dispersion}} + V_{\text{Repulsion}} + V_{\text{Polarization}} \quad (1)$$

$V_{\text{Charge}}$ corresponds to the Coulombic interactions between atomic charges. The second term accounts for the instantaneous correlations of density fluctuations between the electronic clouds (Tesson et al., 2016, 2017):

$$V_{\text{Dispersion}} = -\sum_{i<j}\left[f_6^{ij}(r_{ij})\frac{C_6^{ij}}{(r_{ij})^6} + f_8^{ij}(r_{ij})\frac{C_8^{ij}}{(r_{ij})^8}\right] \quad (2)$$

where $r_{ij}$ is the interatomic distance and the $C_6^{ij}$ and $C_8^{ij}$ terms are the dipole-dipole and dipole-quadripole dispersion coefficients, respectively. The Tang-Toennies function $f^{ij}$ is used for short-range correction:

$$f_n^{ij}(r_{ij}) = 1 - e^{-b_n^{ij}r_{ij}}\sum_{k=0}^{n}\frac{\left(b_n^{ij}r_{ij}\right)^k}{k!} \quad (3)$$

where $k$ and $n$ are integers and $1/b_n^{ij}$ is the range of the dumping.

The repulsion potential is modelled by the following decaying exponential:

$$V_{\text{Repulsion}} = \sum_{i<j} A_{ij}e^{-B_{ij}r_{ij}} \quad (4)$$

where $A_{ij}$ and $B_{ij}$ are two parameters.

Finally, many-body electrostatic effects are described by the induced dipoles $\boldsymbol{\mu}_i$, which are treated as additional degrees of freedom and obtained at each MD step by minimizing the polarization energy,

$$V_{\text{Polarization}} = \sum_{i<j}\left[\frac{q_i\mathbf{r}_{ij}\cdot\boldsymbol{\mu}_j}{r_{ij}^3}g_4^{ij}(r_{ij}) - \frac{q_j\boldsymbol{\mu}_i\cdot\mathbf{r}_{ij}}{r_{ij}^3}g_4^{ij}(r_{ij}) + \frac{\boldsymbol{\mu}_i\cdot\boldsymbol{\mu}_j}{r_{ij}^3}\right. \quad (5)$$

$$\left. - \frac{3\left(\mathbf{r}_{ij}\cdot\boldsymbol{\mu}_i\right)\left(\mathbf{r}_{ij}\cdot\boldsymbol{\mu}_j\right)}{r_{ij}^5}\right] + \sum_i\frac{|\boldsymbol{\mu}_i|^2}{2\alpha_i} \quad (6)$$

where $\alpha_i$ is the polarizability of ion $i$, and $g_4^{ij}(r_{ij})$ are short-range corrections to the multipolar expansion of the Tang-Toennies-type:

$$g_4^{ij}(r_{ij}) = 1 - c_{ij}e^{-b_D^{ij}r_{ij}}\sum_{k=0}^{4}\frac{\left(b_D^{ij}r_{ij}\right)^k}{k!} \quad (7)$$

where $k$ is an integer, $c_{ij}$ a parameter, and $1/b_D^{ij}$ the range of the dumping.

The water model chosen in the parametrization of *PIM* is the Dang-Chang polarizable model (Dang and Chang, 1997), the parameters of which are given in Table S1 of the Supporting Information (SI) file.

The fluorine-clay and fluorine-water parameters $A_{ij}$, $B_{ij}$, $c_{ij}$, and $b_D^{ij}$ have not been published previously and were obtained following the previous procedure (Tazi et al., 2012, Tesson et al., 2016, 2017, 2018) detailed in section 1 of SI. The parameters obtained are given in Table 1.

### *Simulations of contact angles*

Contact-angle simulations were performed with two force fields: *PIM* and the non polarizable force field *ClayFF* (Cygan et al., 2004). The flexible simple point charge *SPC-F* water model (Teleman et al., 1987) was used with *ClayFF* simulations as it was the water model used for the development of *ClayFF*. For fluorine, the same parameters as in Rotenberg et al. (2011) were used.

The simulated systems contained a single layer of hydroxylated or fluorinated talc of formula $Mg_3Si_4O_{10}(OH/F)_2$. The dimensions of the talc surfaces are given in Table 2.

About half of the magnesium atoms located in the middle of the clay layer were fixed during the simulations to prevent clay surfaces from bending. Several drop sizes (i.e. containing different amounts of $H_2O$) were tested. With fewer than 2000 water molecules, it was difficult to obtain spherical drops, especially for the *PIM* force field. In the end, a compromise of 4000 $H_2O$ molecules was the number chosen, which enabled us to obtain spherical drops, with a contact angle independent of the line tension, without lengthening simulation times too much. To ensure that the simulated droplet size was

**Table 1.** Parameters obtained for the interactions between fluorine and the rest of the clay

| | $A_{ij}$ | $B_{ij}$ | $C_6^{ij}$ | $C_8^{ij}$ | $b_n^{ij}$ | $b_D^{ij}$ | $c_{ij}$ | $b_D^{ji}$ | $c_{ji}$ |
|---|---|---|---|---|---|---|---|---|---|
| Ion pairs | (hartree Ha) | ($Å^{-1}$) | ($HaÅ^6$) | ($HaÅ^8$) | ($Å^{-1}$) | ($Å^{-1}$) | (-) | ($Å^{-1}$) | (-) |
| $F^-$–$O^{2-}$ | 103.0 | 3.616 | 0.974 | 5.247 | 2.718 | 5.485 | 6.287 | 3.37 | 2.44 |
| $F^-$–$Mg^{2+}$ | 36.632 | 3.501 | 0.0477 | 0.1556 | 4.1682 | – | – | 3.1632 | 1.3162 |
| $F^-$–$Si^{4+}$ | 980.80 | 3.700 | 0.0477 | 0.1556 | 4.1682 | – | – | 3.8488 | 4.2687 |
| $F^-$–$F^-$ | 8.0478 | 3.4008 | 0.974 | 5.247 | 2.718 | 3.2293 | 4.9823 | 3.2293 | 4.9823 |
| $F^-$–$Ow^{0.82-}$ | 50.011 | 4.5401 | 0.974 | 5.247 | 2.718 | – | – | – | – |
| $F^-$–Mw | – | – | – | – | – | 9.5225 | 3.6214 | 6.9820 | 0.025799 |

https://doi.org/10.1017/cmn.2025.8 Published online by Cambridge University Press

**Table 2.** Simulation box characteristics for the modeling of contact angles on talc surfaces. $L_x$, $L_y$, and $L_z$ are the dimensions of the simulation box along the $x$, $y$, and $z$ axes

| Force field | System | Number of atoms | $L_x$ (Å) | $L_y$ (Å) | $L_z$ (Å) |
|---|---|---|---|---|---|
| *ClayFF* | Talc-OH | 26112 | 147.28 | 109.20 | 500 |
| | Talc-F | 47834 | 214.84 | 209.16 | 500 |
| *PIM* | Talc-OH | 28096 | 134.68 | 143.52 | 500 |
| | Talc-F | 51834 | 214.84 | 209.16 | 500 |

sufficient, a simulation of a cylindric droplet on a talc-OH surface was also conducted with *ClayFF* force field. The simulation details are given in section 3 of the SI. The contact angle showed no significant difference from that obtained from spherical droplets.

All the simulations were performed in the the canonical ensemble at a temperature of 300 K with a timestep of 1 fs. Long-range electrostatic interactions were computed with Ewald summation. The simulation codes *Metalwalls* (Marin-Laflèche et al., 2020) and *LAMMPS* (Plimpton, 1995) were used with *PIM* and *ClayFF* force fields, respectively. For 2 ns, the water molecules were trapped in a cube made of virtual walls specified by a repulsive Lennard Jones to keep them close to the surface. The walls were removed and the systems were equilibrated for a further 1 ns. The atoms' positions were recorded every 1000 timesteps for a total of 4 ns and used to calculate the contact angles.

The 2-dimensional density $\rho(z,r)$ (Fig. 2) was extracted from the positions with a home-made program, where z is the height from the first atomic plane of the clay surface and r is the radial distance to the drop's center of mass. The liquid–vapor interface was characterized by the blue points where the local density was equal to half the bulk density $\rho_0$, which was defined by the red square in the drop's center. A circle segment was fitted to the blue dots, and the contact angle was calculated by intersecting the circular fit with the interface plane. Like the experimental contact-angle values, the simulated ones depend on the distance to the surface from which the tangential line was drawn. The impact of the choice of the water–clay interface on the contact angle value is illustrated in Fig. 2. As in the experiment, two extreme base lines could be considered: the first was situated at the $z$ position of the surface atoms and the second at $z$ position of the first water oxygen atoms. The distance between these two baselines was ~3–3.5 Å, which corresponded to ~8–10% of the drop radius. This percentage is close to its experimental equivalent, resulting in a range of angles of 3 to 6°. The baseline chosen to evaluate the contact angle was located at the mean distance between the two extreme baselines, as for experiments.

## Results

### *Experimental contact angles*

The final result was averaged over 54 measurements, resulting in a value of 80.3° with a standard deviation of 2.3°. A histogram of the distribution of the measured contact angle is given in Fig. S2 of SI. This value was compared with literature values given in Table 3.

Measurements of advancing and receding contact angles on a macrocrystal of talc were made by Yin and Miller (2012), obtaining angles of 69° and 75°, respectively, indicating a slightly hydrophilic behavior of the surface. However, no information on drop volume or in terms of the number of measurements was provided. In addition, it is unusual to observe an advancing angle which is greater than the receding angle. It is likely that the authors mistakenly reversed the order of the values.

**Table 3.** Summary of different water contact-angle studies on various talc samples

| System | Method | Contact angle (°) | Reference |
|---|---|---|---|
| Monocrystal | sessile drop | $\theta_a$ :69 $\theta_r$ :75 | Yin and Miller (2012) |
| Monocrystal | sessile drop | 90 ± 3 | Kaggwa et al. (2006) |
| Powder | washburn | 80 ± 2 | |
| Monocrystal | sessile drop | 79 ± 2 | Atluri et al. (2019) |
| Monocrystal | sessile drop | $\theta_a$ :60 $\theta_r$ :50 | Douillard et al. (2002) |
| Powder | washburn | 80.4 ± 1.6 | Giese et al. (1991) |
| Powder | washburn | 87 | Yuan et al. (2018) |
| Film | sessile drop | 75 | Liimatainen et al. (2013) |
| Monocrystal | sessile drop | 80.3 ± 2.3 | This study |

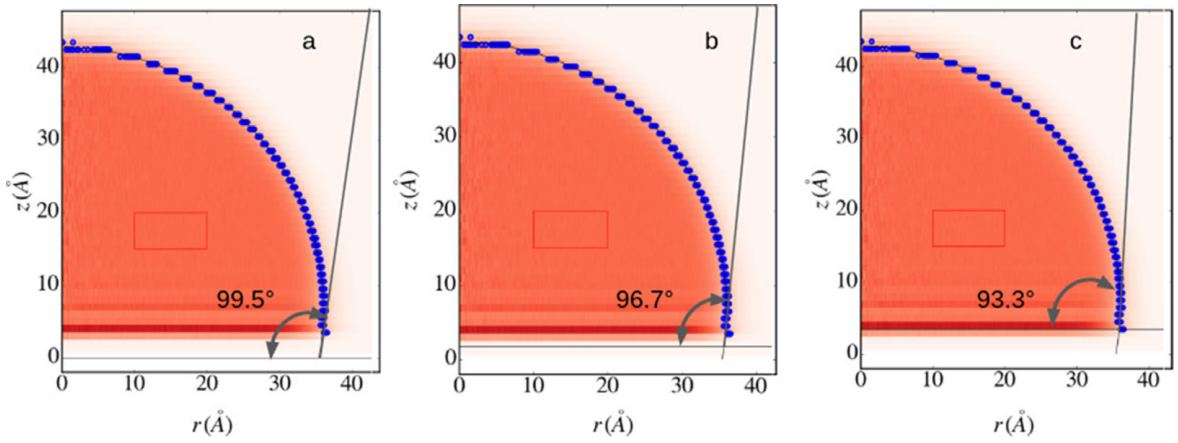



**Figure 2.** Representation of the contact-angle measurement from the density profiles of droplets extracted from molecular dynamics trajectories and the influence of the baseline placement on the measured contact angle values. The density profiles were extracted from the simulations performed on hydroxylated talc modeled by *ClayFF*. The same procedure was applied with *PIM*. The blue circles correspond to the positions where the water density is equal to half of the density of water in the droplet.

https://doi.org/10.1017/cmn.2025.8 Published online by Cambridge University Press

Talc wettability was studied (Kaggwa et al., 2006) by measuring contact angles on both a single crystal and powders. They deposited ultrapure water droplets with a volume of 100 μL on a freshly cleaved surface using a micropipette. After only five static angle measurements, the average measured angle was 90 ± 3 °. Contact-angle measurements on powders were performed using the Washburn method (Washburn, 1921), resulting in a contact angle of 80 ± 2 °. Kaggwa et al. (2006) explained the 10° discrepancy between these two measurements as being due to the hydrophilic edges of talc particles present in the powders, whereas only the basal surface of talc is considered in the sessile drop method on a single crystal.

An advancing angle of 60° and a receding angle of 50° were measured by Douillard et al. (2002) on a single crystal of talc. Their values are significantly lower than others, which can be explained by the fact that their talc surface was polished rather than freshly cleaved, potentially leading to surface contamination.

A static contact angle of 75 ± 2 ° on thin talc films made from powder was measured by Liimatainen et al. (2013). In the case of talc films, surface roughness is significant, and the contact angle may appear lower due to the presence of hydrophilic sites on the edges of clay particles.

An angle of 87° was obtained using the Washburn method (Yuan et al., 2018), while a contact angle of 80.4 ± 1.6 ° was measured by Giese et al. (1991), also using the Washburn method.

According to the literature, and even taking into account the variability in experimental procedures and the statistical uncertainty associated with such measurements, the contact angle of water on talc generally ranged from 75° to 90°. The average angle of 80.3° measured in this study was thus consistent with most literature values. Still, it is possible that the partial peeling of the monocrystal may have generated steps, resulting in a lower contact angle than might be expected on an ideal surface. Indeed, depending on the surface, it has been shown that roughness can either increase (Cassie and Baxter, 1944; Wenzel, 1936) the contact angle with the combined effect of the geometry of the surface and the surface tension of the liquid or reduce it (Wenzel, 1936) by offering more sites for adhesion. The (010) plane of clays being more hydrophilic than the basal plane (Du and Miller, 2007; Nalaskowski et al., 2007; Yin and Miller, 2012), significant roughness and large steps should lead to a smaller apparent contact angle than the contact angle that would be obtained on an ideal surface but still closer to reality than contact angles obtained with samples of talc powder.

### *Simulated water contact angles and comparison with experimental data*

Calculated contact angles are reported in Table 4, together with the experimental contact angle.

Although no contact-angle simulations have been carried out previously using *PIM*, the values found for hydroxylated and fluorinated talc with *ClayFF* were consistent with those reported by Rotenberg et al. (2011), i.e. 96° and 103°, respectively, using *ClayFF* and *SPC/E* as the water model. Atluri et al. (2019) also simulated water droplets on talc surfaces using molecular dynamics with the *ClayFF* force field and the *SPC/E* water model. Those authors observed a contact angle of 70° after only 1 ns of simulation including equilibration, which was a relatively short simulation time. Generally, simulated droplets require a few nanoseconds to reach a stable state (Ravipati et al., 2018).

Changing the force field had no drastic impact on the value of the contact angles, and the contact angle obtained for both forcefields in the case of hydroxylated talc were larger than experimental data. This may be partially explained by the fact that simulated surfaces were perfectly flat and devoid of defects, while the crystalline surface in the experiment was rough with large steps. Another interpretation was that neither force field chosen was good enough to provide a quantitative agreement with experiment.

Nevertheless, even if direct comparison between experiment and simulation was rather difficult in view of the defects in the sample, the angle given by *PIM* was closer to the experimental data than the *ClayFF*. Moreover, for the same force field, the contact angle on fluorotalc was greater than on the hydroxylated talc. Both force fields thus demonstrated the hydrophobic character of fluorine, as observed experimentally (Dazas et al., 2013; Michot et al., 1994). However, the difference remained moderate considering the differences observed in the amount of interlayer water in charged clays, depending on whether they are hydroxylated or fluorinated (Dazas et al., 2013; Marry et al., 2011).

The differences in contact angles calculated with the two force fields could be multi-factorial. If the force field chosen for the clay could play a role, e.g. polarizability, water properties could also differ from one water model to another. In the next section, the impact of the force field on the fluid is examined in more detail.

**Table 4.** Measured and calculated contact angles for the present study. The value in parentheses represents the contact angle calculated for the cylinder droplet on a talc-OH surface using the *ClayFF* force field (see text and section 3 of SI)

| Clay | *PIM* | *ClayFF* | Experimental |
|---|---|---|---|
| Talc-OH | 94.3 ± 0.4° | 96.7 ± 0.2° (98.1 ± 0.8°) | 80.3 ± 2.3° |
| Talc-F | 98.3 ± 0.6° | 100.2 ± 0.03° | – |

### *Structure of the fluid at the solid–liquid interface: comparison of the two force fields*

To study the structural organization of water at the water–clay interface, the atomic distributions of water oxygens with respect to the different surfaces were studied (Fig. 3). To avoid taking into

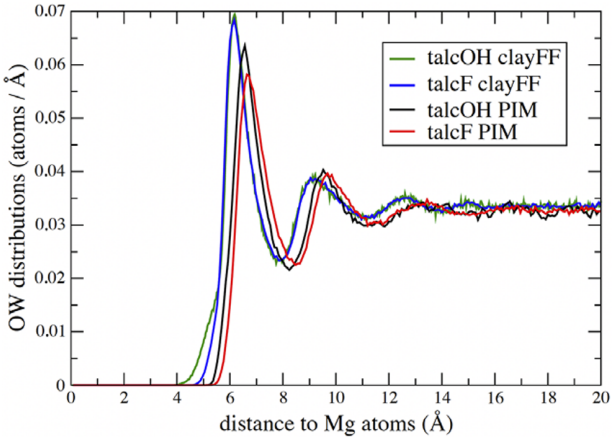



**Figure 3.** Atomic distributions of the oxygen atoms of the water molecules (OW) in the direction perpendicular to the talc surfaces. Black: talc-OH with *PIM*, Green: talc-OH with *ClayFF*, Red: talc-F with *PIM*, Blue: talc-F with *ClayFF*. The two curves obtained with *ClayFF* were the same, except for the shoulder in the case of talc-OH at ~5 Å. The distance to the surface was calculated as the difference between the vertical position *z* of the OW atoms and that of the Mg atoms in the middle of the clay layer.

https://doi.org/10.1017/cmn.2025.8 Published online by Cambridge University Press

account water molecules at the water–vapor interface that may have behaved differently from molecules at the heart of the drop, only molecules located inside a cylinder of radius 25 Å, the axis of which, perpendicular to the surface, passed through the drop's center of gravity, were taken into account.

The presence of peaks close to surfaces was a sign of layered water structuring, which is commonly present on the surface of many materials, even hydrophobic ones (Jamadagni et al., 2011; Monroe et al., 2020). As revealed in Fig. 3, water molecules were located closer to the surface for *ClayFF* than for *PIM*. Furthermore, the first distribution peak was less intense in the case of *PIM* than *ClayFF*. It has already been observed that *PIM* induced a more disordered organization of water molecules compared to the *ClayFF* force field, probably responsible for the slightly better reproduction of XRD patterns with *PIM* model (Hånde et al., 2018; Tesson et al., 2018). On the other hand, the first minimum at ~8 Å and second peak at ~9–10 Å were more pronounced in *PIM*, suggesting longer-range fluid structuring.

For *PIM*, fluorinated talc repelled water molecules slightly further than hydroxylated talc, and the first peak was less pronounced. For *ClayFF*, distributions were very similar for both talcs with the exception of a pronounced shoulder near the surface in the case of hydroxylated talc. The Si-O-Si basal surface of talc has already been shown to be rather hydrophobic, the OH sites of the hydroxylated talc being the only hydrophilic parts that account for the adsorption of more water at low relative humidity on talc-OH compared with talc-F (Michot et al., 1994; Rotenberg et al., 2011). The hydroxyl group may add, through the presence of an additional dipole, an overall attraction with the fluid, which translates differently depending on the force field. In the case of *ClayFF*, the orientation of the hydroxyl group, which depends on whether the layers are trioctahedral or dioctahedral, or its replacement with fluorine, was shown to have an effect on water at the interface (Bourg et al., 2017; Koishi et al., 2022). However, this effect was observed with mica surfaces which are highly charged clays, where the electrostatic field at the surface orients water molecules with their hydrogen toward the surfaces. Consequently, these results are not directly comparable to the results of the present study. In the case of *PIM*, a detailed study of the induced atomic dipoles could perhaps provide a better understanding of the effect of replacing the hydroxyl with fluorine.

Distribution maps parallel to the clay layers were calculated for oxygen (OW) and hydrogen (HW) atoms of $H_2O$ molecules contained in the first peak of the vertical distributions. They are shown in Fig. 4 for talc-OH. The maps were reduced to a unit cell represented schematically on the figure by its surface O (in red) and Si (in yellow) atoms. For *ClayFF*, the distributions of HW in the shoulder of the first distribution peak were also plotted.

For both force fields, the OWs tended to be positioned above the surface Si and especially above the centers of the hexagonal cavities. The distributions for both force fields had characteristics similar to those obtained on the surface of montmorillonite, a charged clay (Le Crom et al., 2020). However, the preferential positions were less pronounced than in the case of charged clays, especially in the case of *PIM* force field, because in charged clays, $H_2O$ molecules orient themselves toward the surface to form hydrogen bonds with surface O atoms under the action of the electrostatic field created by the charges. The difference in intensity of OW distributions at the center of the cavity between the two force fields (slightly more intense for *ClayFF* than for *PIM*) was only due to $H_2O$ contained in the shoulder of *ClayFF* first peak distribution (Fig. 3). Indeed, these molecules featured pronounced structuring, as evidenced by the distribution of their HW atoms along the surface. In the case of talc-F (Fig. S3), no such structural organization is observed. On the other hand, there was an overconcentration of HW above the center of the cavity in the case of *PIM*. It corresponded to $H_2O$ located above hexagonal cavities, with an OH bond perpendicular to the clay layer pointing its H towards the center of the cavity. This overconcentration remained in the case of talc-F, albeit to a lesser extent (Fig. S4).

The preferential orientations were reflected in the distributions of $H_2O$ orientations. The orientation of a water molecule was defined by the angles θ and β between the dipole vector μ and the dipole perpendicular to the plane of the molecule $\mathbf{n}$ and perpendicular to the clay layer respectively, as shown on Fig. 5. When plotting cosβ as a function of cosθ for the molecules contained in the first peak of OW distribution, the two maps shown on Fig. 5 were obtained for talc-OH.

The greatest probability was obtained at $\theta \approx 90°$ and $\beta \approx 0°$, corresponding to molecules parallel to the surface. More generally, the preferential orientations seen on the circle $\cos^2\beta + \cos^2\theta = 1$ corresponded to molecules with the plane defined by their two vectors $\boldsymbol{\mu}$ and $\boldsymbol{n}$ perpendicular to the surface. Note that in the case of *ClayFF*, the few water molecules contained in the shoulder of the distribution peak (see Fig. 3) had their maximum probability on this circle, around $\cos\theta = 0.4$, or $\theta = 65°$ (Fig. S5). This corresponded to molecules with their two hydrogens slightly oriented towards the fluid and located at the same height. A relative maximum probability was also obtained around $\cos\theta = 0.6$ and $\cos\beta = 0$ for the two force fields, corresponding to a water molecule pointing an H vertically toward the fluid. A notable difference between the two force fields was the presence of a relative maximum for *PIM* at values $\cos\theta = -0.6$ and $\cos\beta = 0$. These values corresponded to water molecules pointing an H vertically towards the surface. These molecules were precisely those already observed on horizontal distributions pointing their H toward the center of the hexagonal cavities.

In the case of *PIM*, the distributions parallel to the clay surface with talc-F showed similar characteristics, although a little less marked. The main difference was for *clayFF* because the absence of water molecules in the cavities eliminated HW structuring and reduced the intensity of the OW distribution in the center of the cavities (Fig. S3). The orientations obtained with fluorinated talc were very similar to those in Fig. 5 and are not presented here.

## Discussion

One of the thermodynamic quantities usually used to characterize the wetting behavior of a liquid on a solid surface is the work of adhesion, defined as the work per unit area required to remove a liquid from a solid surface:

$$W_{SL} = \gamma_{SV} + \gamma_{LV} - \gamma_{SL} \tag{8}$$

where $\gamma_{SV}$ is the solid–vapor interfacial tension, $\gamma_{SL}$ the solid–liquid interfacial tension and $\gamma_{LV}$ the liquid surface tension.

Using Young's equation (Young, 1805) which links the contact angle of a droplet of liquid on a solid surface with interfacial tensions:

$$\gamma_{LV}\cos\theta = \gamma_{SV} - \gamma_{SL} \tag{9}$$

https://doi.org/10.1017/cmn.2025.8 Published online by Cambridge University Press

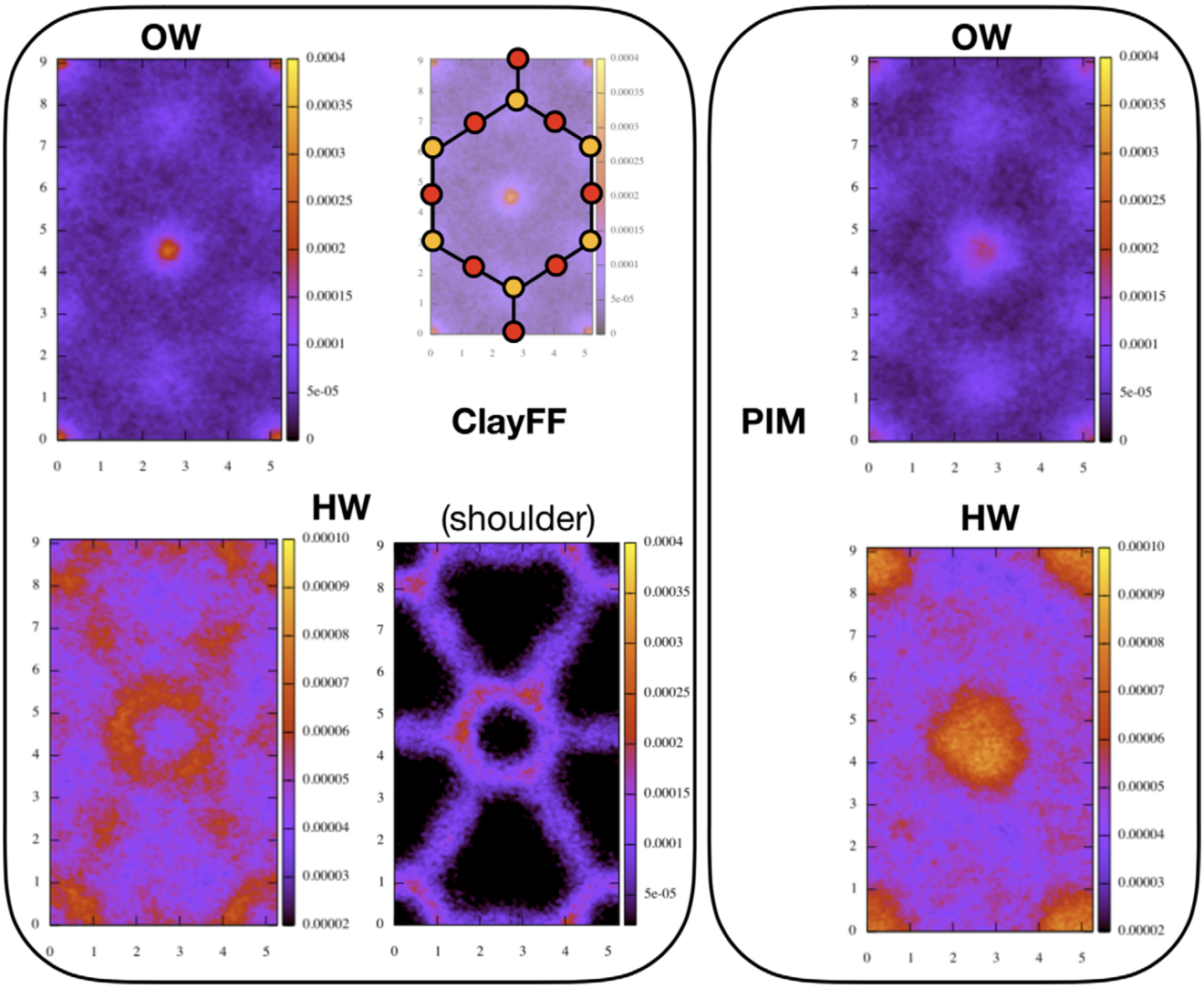



**Figure 4.** Atomic distributions of OW and HW in talc-OH, parallel to the surface and reduced to a unit cell, represented schematically by its surface O (in red) and Si (in yellow) atoms, shown at a smaller size in the left frame. The color scale goes from black (corresponding to the absence of atoms) to yellow (maximum concentration). Maximum concentrations were set at the same value for both force fields for each atom type. Only the scale for HW contained in the shoulder of the first distribution peak for *ClayFF* only (bottom right of the left frame) is different.

and knowing $\gamma_{LV}$, the work of adhesion can be calculated directly from the contact angle:

$$W_{SL} = \gamma_{LV}(1 + \cos\theta) \tag{10}$$

Experimentally, measuring the contact angle of a drop deposited on a surface is the most direct way of obtaining $W_{SL}$. On the other hand, molecular simulations provide various ways of calculating $W_{SL}$, including the measure of a contact angle on a solid surface. Bistafa et al. (2021) have shown that these different methods give similar values of $W_{SL}$ to within a few percent for flat surfaces.

From statistical thermodynamics developments, it can be shown that $W_{SL}$ depends only on solid/liquid interactions as:

$$W_{SL} = -\langle u_{SL}\rangle - T\Delta s_{SL} \tag{11}$$

where $\langle u_{SL}\rangle$ is the mean solid–liquid interaction energy per unit area and has negative value. The minus sign in equation 11 comes from the fact that these interactions must be overcome to separate the liquid from the solid. $\Delta s_{SL}$ is the corresponding entropy increase upon the solid/liquid separation. As a result, $W_{SL}$ is the sum of a positive energetic term and a negative entropic term. It has been shown in the literature that two systems with the same average potential energy $\langle u_{SL}\rangle$ but different types of interaction (Lennard-Jones vs. Coulomb) could exhibit quite different work of adhesion values, with Coulomb interactions accentuating the entropy loss $-\Delta s_{SL}$ due to the presence of the interface and leading to smaller work of adhesion and then bigger values of θ (Surblys et al., 2018).

From a thermodynamic point of view, in order to understand the differences observed between force fields and experiment, it makes more sense to compare works of adhesion rather than contact angles. Indeed, while the work of adhesion is linked directly to the interactions between solid and liquid (equation 11), contact angle also depends on the interfacial tension of water, which can differ from one water model to another (equation 10). Then the interfacial tension of the two water models used in the present study were first calculated: flexible *SPC* for *ClayFF* (Teleman et al., 1987) and Dang-Chang for *PIM* (Dang and Chang, 1997). The method used to calculate these interfacial tensions is given in section 6 of SI. The

https://doi.org/10.1017/cmn.2025.8 Published online by Cambridge University Press

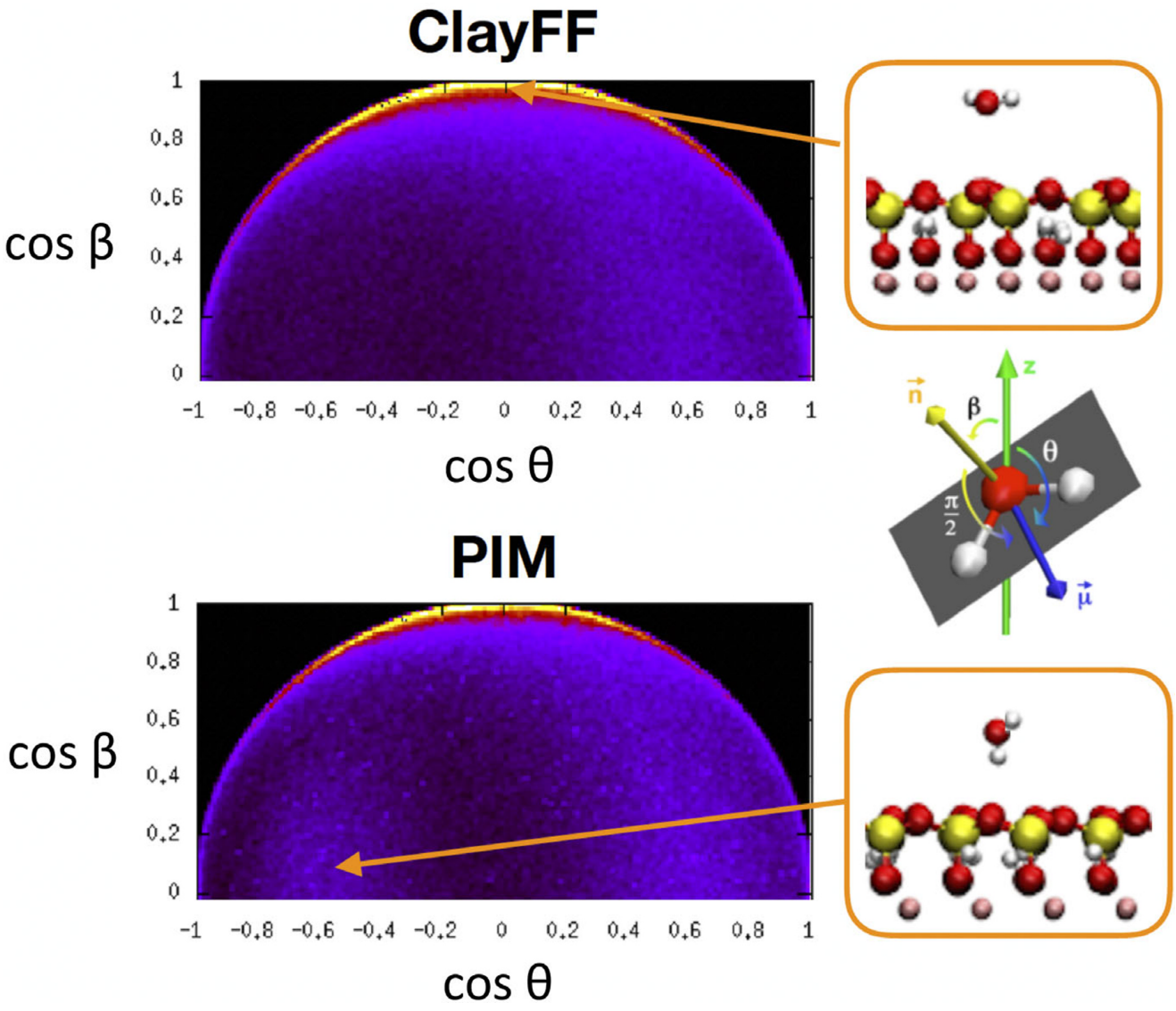



**Figure 5.** Orientational distributions for water molecules in the first distribution peak, i.e. the closest to the talc-OH surface. θ and β angles are defined on the diagram in the middle. The color scale is the same for both maps. It goes from black (zero probability) to yellow (maximum probability).

calculated and experimental surface tension values are reported in Table 5. The value of $\gamma_{water-air}$ obtained with the flexible *SPC* model was within the range of surface tensions obtained with other flexible models (52-70 mN/m) (Yuet and Blankschtein, 2010). For the Dang-Chang model, the obtained $\gamma_{water-air}$ value was well below that found by Dang and Chang (1997), i.e. 92 mN/m, but in their original article, the authors cut the interactions at 9 Å, without using the Ewald sum for coulombic interactions, and the simulation time was short (300 ps).

**Table 5.** Water–air interfacial tension calculated for both water models used in this study. The works of adhesion values have been calculated with $\gamma_{water-air}$ estimated with the highest cutoff. Error bars include $\gamma$ and contact angle errors

| Water models | $\gamma_{water-air}$ (mN.m$^{-1}$) | $W_{SL}$ talc-OH (mN.m$^{-1}$) | $W_{SL}$ talc-F (mN.m$^{-1}$) |
|---|---|---|---|
| *SPC-Fw* | 61.7 ± 1.7 | 54.5 ± 1.7 | 50.8 ± 1.5 |
| Dang-Chang | 65.1 ± 1.5 | 60.2 ± 1.8 | 55.7 ± 2.0 |
| Experimental | 72 | 84.5 | |

Using the $\gamma_{water-air}$ values in Table 5 and contact angles values in Table 4, values for work of adhesion were calculated. They followed the same trends as contact angles (the greater the contact angle, the smaller the work of adhesion), except for talc-F with *PIM* which had a slightly greater work of adhesion than talc-OH with *ClayFF*, although the contact angle was slightly greater. These values were nevertheless very close, and this difference, due to the different values of $\gamma_{water-air}$ did not change the qualitative conclusions: for both force fields, the work of adhesion was smaller for talc-F than for talc-OH. Moreover, both force fields yielded smaller values of works of adhesion than the experiment, i.e. the simulated surfaces were more hydrophobic, even though *PIM* was a little closer to the experiment.

Nevertheless, given that the error bars on $W_{SL}$ were of the order of 2 mN.m$^{-1}$, i.e. only slightly smaller than the difference between $W_{SL}$ obtained for the different systems, the results were checked by calculating the difference in $W_{SL}$ between talc-OH and talc-F in

https://doi.org/10.1017/cmn.2025.8 Published online by Cambridge University Press

another way, at least for *ClayFF*, using the alchemy command available in *LAMMPS*. Along a single simulation, the hydroxyl groups of the talc-OH were transformed into fluorine in order to calculate a free energy difference $\Delta F(\mathrm{OH}\rightarrow\mathrm{F})$. This transformation was done for dry and wet talc and the $\Delta W_{SL} = W_{SL}^{F} - W_{SL}^{OH}$ was therefore obtained from the difference between wet and dry $\Delta F$. The procedure used is described in section 7 of SI. Using this procedure, a value for $\Delta W_{SL} = -3.1 \pm 0.2$ mN.m$^{-1}$ was obtained, which was a little smaller in absolute value than the value obtained with contact angles, i.e. -3.7 mN.m$^{-1}$, but it confirmed the order of magnitude and supports the conclusion that the fluorinated talc was slightly more hydrophobic than the hydroxylated one.

The work of adhesion is linked directly to the interaction energy between water and the surface through the first term of equation 11. In the case where solid–water interactions were represented by Lennard-Jones only, previous works showed an almost proportional relationship between $W_{SL}$ and $-\langle u_{SL}\rangle$ that was independent of the type of surface and water model (graphite, graphene, silica) (Leroy et al., 2015; Surblys et al., 2018). As a result, the negative entropic term $-T\Delta S_{SL}$ in equation 11 was also almost proportional to $-\langle u_{SL}\rangle$ and its absolute value increased with $-\langle u_{SL}\rangle$: the more the liquid was attracted by the solid, the more the fluid was constrained to the surface and lost entropy. However, this entropy loss varied according to the type of interaction between fluid and solid. Thus, for two interfaces with the same interaction energy $\langle u_{SL}\rangle$, the entropic term could be very different, depending on whether the interaction between the solid and the fluid molecules was of the Lennard-Jones type only, or whether there were also coulombic interactions (Surblys et al., 2018). In the latter case, the entropy loss was greater and the work of adhesion smaller. Separating the energy term from the entropy term requires calculation of $-\langle u_{SL}\rangle$. Such a calculation is not straightforward, as it requires separation of the different energy terms according to the different groups of atoms in the overall energy calculation, a procedure that is not implemented in *Metalwalls*. Still, $-\langle u_{SL}\rangle$ could be calculated with *LAMMPS*, in the case of *ClayFF* force field. Values of $-\langle u_{SL}\rangle = 92.7$ mN.m$^{-1}$ for talc-OH and 80.1 mN.m$^{-1}$ for talc-F were found, which indicated that the attraction between water and talc was stronger when talc was hydroxylated. From $W_{SL}$ and $\langle u_{SL}\rangle$, the loss of entropy linked to the formation of the solid/liquid interface could be calculated: $-T\Delta s_{SL} = -38.2$ mN.m$^{-1}$ and $-29.3$ mN.m$^{-1}$ for talc-OH and talc-F respectively. Entropy loss actually increased (in absolute value) as the energy of attraction between solid and fluid increased. A similar trend was also observed in highly charged clays such as micas (Koishi et al., 2022).

When these results were compared with those obtained by other teams who have worked on similar surfaces, i.e. moderately hydrophobic, striking analogies could be found. In particular, Surblys et al (2018) studied in detail the dependence of work of adhesion and entropy loss on the intensity of interatomic interactions at the interface between silica ($SiO_2$) and water. By progressively turning on the Lennard-Jones interactions between solid and fluid with a coupling parameter κ such that $V_{LJ} = \kappa(4\varepsilon_{ij}[\sigma_{ij}^{12}/r_{ij}^{12} - \sigma_{ij}^{6}/r_{ij}^{6}])$(κ ranging from almost 0 to 2), then the coulombic interactions with a coupling parameter λ, such as $V_{Coulomb} = \lambda\sum_{i,j} q_i q_j/(4\pi\varepsilon_0 r_{ij})$ (λ ranging from 0 to 2), they were able to study the evolution of $W_{SL}$ and $-T\Delta s_{SL}$ with increasing values of $-\langle u_{SL}\rangle$ corresponding to various couples (κ, λ). In particular, they found that $W_{SL}$ and $-T\Delta s_{SL}$ were different affine functions of $-\langle u_{SL}\rangle$ depending on whether κ was varied while λ was fixed to 0 (i.e. varying LJ interactions and no coulombic interactions), or λ was varied while κ was fixed to 1 (i.e. varying coulombic interactions and full LJ interactions). So two systems (κ, 0) and (1, λ) having the same average interaction energy $-\langle u_{SL}\rangle$ had different $W_{SL}$ and $-T\Delta s_{SL}$. To be more precise, the system with Lennard-Jones interactions only (corresponding to (κ, 0)) had a lower entropy loss and therefore greater work of adhesion.

Surprisingly the values of $W_{SL}$ and $-T\Delta s_{SL}$ for both talcs simulated with *ClayFF* were located on exactly the same linear function as Surblys et al. (2018), i.e. that corresponding to a λ that varied, with the value of κ fixed at 1. More precisely, $W_{SL}$ and $-T\Delta s_{SL}$ were the same for talc-F and the couple (κ = 1, λ = 1), which corresponded to the silica/water interface with full Lennard-Jones and full coulombic interactions. In comparison, values for talc-OH corresponded to silica–water interface with coupling parameters κ = 1 and λ = 1.4, i.e. full LJ interactions and increased coulombic interaction compared to silica–water interface. As both solid surfaces (silica and talc) are made of silicon oxide, with oxygens slightly closer to the fluid than silicons, it was reasonable to assume that the effects of both surfaces on water were similar, even if Si-O-Si patterns on the surface were different. Moreover, as Lennard-Jones interactions are short-range, they are governed more by surface atoms in direct contact with the fluid. These two reasons may explain why the two talcs had same $W_{SL}$ and $-T\Delta s_{SL}$ values as silica with full Lennard-Jones interactions (κ = 1). The effect of OH/Fs located deeper in the talc layer on the fluid was more likely to be of coulombic origin: the presence of the additional dipole due to the hydroxyl group (with its H oriented towards the surface) would be at the origin of an additional attraction responsible for the shoulder visible on the OW distributions which would explain the increased value of λ for talc-OH.

Consider now the results obtained with the *PIM* force field. Even if the $\langle u_{SL}\rangle$ energy in the case of the *PIM* polarizable force field could not be calculated, the results could, nevertheless, be commented on, in the light of Surblys' (2018) work on silicas. The structure of the fluid at the interface reflected to some extent the attraction of the fluid to the surface. When similar systems with the same types of interactions were compared, the greater the interaction, the closer the fluid was expected to approach the surface (Godawat et al., 2009), and the greater the distribution peaks, particularly the first peak (Maibaum and Chandler, 2007). However, the distribution of molecules in the vicinity of the surface varied significantly with the type of interactions between the fluid and the surface. Surblys thus obtained very different OW distributions for silicas with LJ interactions only (λ fixed to 0) and with mixed LJ and coulombic interactions (κ fixed to 1). For two systems having the same average interaction energy $\langle u_{SL}\rangle$, Lennard-Jones interactions gave distribution peaks further from the surface, but also more pronounced than a mixture of Lennard-Jones and Coulombic interactions. Similar differences were also observed when comparing profiles obtained with *PIM* and *ClayFF*. The fact that *PIM* gave profiles further from the surface was not synonymous with less attraction.

Nevertheless, regardless of the interaction, Surblys also found that the surface density of water in the surface layer (corresponding to the number of water molecules in the first adsorption layer per surface unit) increased with $-\langle u_{SL}\rangle$ and followed the same increasing function of $-\langle u_{SL}\rangle$ regardless of the intensity and type of solid/liquid interaction (LJ only or mixed LJ and coulombic interactions). By counting the number of water molecules contained in the first distribution peaks, average surface densities $\langle n_{ads}\rangle$ of 10.7 and 10.4 molecules per nm$^2$ for *ClayFF* in talc-OH and

https://doi.org/10.1017/cmn.2025.8 Published online by Cambridge University Press

talc-F respectively, and 9.8 and 9.4 molecules per nm$^2$ for *PIM* in talc-OH and talc-F, respectively, were obtained: a greater density for *ClayFF* than for *PIM* (which was consistent with a more intense first peak in *ClayFF* distributions) suggested a lower interaction energy $-\langle u_{SL}\rangle$ for *PIM* than for *ClayFF*. If this assumption was correct, then the origin of the larger value for work of adhesion obtained with *PIM* was necessarily entropic, in the same way that silicas interacting with the fluid via LJ potentials alone caused an entropy loss of the fluid lower than that interacting via a mixture of LJ and coulombic potentials. It could be assumed therefore that the fluid was less constrained, and therefore lost less entropy when located further away from the surface, as was the case for *PIM* and for silicas with LJs interactions only.

The measurement of local density fluctuations at the surface has often been used to characterize the solvophobicity of surfaces: the more solvophobic a surface, the greater the local fluctuations (Acharya et al., 2010; Ashbaugh et al., 2021; Evans and Stewart, 2015; Jamadagni et al., 2011; Wilding et al., 2024; Willard and Chandler, 2014). The fluctuations in the number of water molecules in the surface layer containing the first peak of distribution of OW atoms were calculated. The values obtained were $\langle(n_{\text{ads}} - \langle n_{\text{ads}}\rangle)^2\rangle/\langle n_{\text{ads}}\rangle =$ 0.180 and 0.179 for talc-OH and talc-F simulated with *ClayFF* respectively, and 0.169 and 0.173 for talc-OH and talc-F simulated with *PIM* respectively. The fluctuations were noticeably lower in the case of *PIM*, which was consistent with a more hydrophilic surface with this force field.

## Conclusions

Two talcs, hydroxylated and fluorinated, were studied in a first attempt to understand the difference in hydrophilicity due to the exchange of the hydroxyl group by fluorine, observed in a number of clays.

To this end, careful measurements of contact angles on single crystals were undertaken, as well as molecular simulations with two different force fields (one non-polarizable and one polarizable). Whatever the force field used, the calculated contact angles overestimated values found by experiment. Moreover, fluorinated talc was found to be slightly more hydrophobic than hydroxylated talc for both of the force fields considered. Despite the fact that the properties of the fluid at the interface were quite, or even very different between the force fields, the contact angles (and related work of adhesion values) remained quite close to each other, and similar to those obtained on similar silica-type surfaces. This would seem to indicate that obtaining smaller angles in the case of experiment was due to the presence of steps on monocrystal surfaces, which rendered the real surface more hydrophilic than the ideal one.

When comparing the two force fields, it is obvious that the density of water near a surface was not a good indicator of the surface's hydrophilicity: despite the fact that the density peaks were closer to the surface and more intense in the case of *ClayFF*, *ClayFF* produced the most hydrophobic surfaces. Indeed, more depletion close to the surface in the case of *PIM*, which could be the sign of less attraction between the fluid and the solid on one hand, could be responsible for less contraint for the fluid on the other hand, leading to less entropy loss and therefore to greater work of adhesion. Then, although the two force fields finally produced relatively close contact angles, the properties of the fluid at the interface were significantly different from a thermodynamic point of view, and in particular from the point of view of the balance between energy and entropy.

In the future, the differences in hydrophilicity between charged clays will be investigated, in particular to understand the origin of the more hydrophobic behavior of fluorinated clays compared with hydroxylated clays (Malikova et al., 2007; Michot et al., 1994). In the case of charged clays, which are more hydrophilic due to the presence of counter ions on their surface, the contact angle is not a good indicator because the drop spreads over the surface. Other methods, such as the thermodynamic integration used in the present article (see Supplementary Information, section 'Alchemy transformation with C*layFF* force field') will then have to be considered in order to calculate differences in free energy between clays containing F or OH, or different cations. Note that it could also be interesting to test force fields other than those in the present study, such as the recently developed *ReaxFF* for use with earth materials (Gao et al., 2024; Zhang et al., 2024).

**Supplementary material.** The supplementary material for this article can be found at http://doi.org/10.1017/cmn.2025.8.

**Author contributions.** L. Guérin carried out the experimental measurements under the direction of L. Michot and the molecular dynamics simulations of contact angles under the direction of V. Marry. T. Bernhard carried out the thermodynamic integration to determine the work of adhesion under the supervision of V. Marry. E. Ferrage provided the talc samples and supervised and advised L. Guérin throughout this work, as did F. Claret. All authors provided quality feedback and significantly influenced the research and manuscript.

**Acknowledgements.** This work was granted access to the HPC resources of IDRIS under the allocation 2021-A0100412473 made by GENCI. The authors are grateful to the CNRS interdisciplinary 'défi Needs' program (Project DARIUS). V. Marry thanks R. Vuilleumier for fruitful discussions.

**Financial support.** L. Guérin's work was funded by the CNRS interdisciplinary 'défi Needs' program (Project DARIUS).

**Competing interests.** The authors declare that they have no competing interests.

## References

Acharya, H., Vembanur, S., Jamadagni, S. N., & Garde, S. (2010). Mapping hydrophobicity at the nanoscale: Applications to heterogeneous surfaces and proteins. *Faraday Discussions*, *146*, 353–365. https://doi.org/10.1039/B927019A

Ashbaugh, H. S., Vats, M., & Garde, S. (2021). Bridging gaussian density fluctuations from microscopic to macroscopic volumes: Applications to non-polar solute hydration thermodynamics. *The Journal of Physical Chemistry B*, *125*(29), 8152–8164. https://doi.org/10.1021/acs.jpcb.1c04087

Atluri, V., Jin, J., Shrimali, K., Dang, L., Wang, X., & Miller, J. D. (2019). The hydrophobic surface state of talc as influenced by aluminum substitution in the tetrahedral layer. *The Journal of Colloid and Interface Science*, *536*, 737–748. https://doi.org/10.1016/j.jcis.2018.10.085

Bistafa, C., Surblys, D., Kusudo, H., & Yamaguchi, Y. (2021). Water on hydroxylated silica surfaces: Work of adhesion, interfacial entropy, and droplet wetting. *The Journal of Chemical Physics*, *155*(6), 064703. https://doi.org/10.1063/5.0056718

Bourg, I. C., Lee, S. S., Fenter, P., & Tournassat, C. (2017). Stern layer structure and energetics at mica–water interfaces.*The Journal of Physical Chemistry C*, *121*(17), 9402–9412. https://doi.org/10.1021/acs.jpcc.7b01828

Brigatti, M. F., Galan, E., & Theng, B. (2006). Structure and mineralogy of clay minerals. In: F. Bergaya & G. Lagaly (Eds.), *Handbook of clay science 1*. Elsevier, Amsterdam.

Cassie, A. B. D., & Baxter, S. (1944). Wettability of porous surfaces.*Transactions of The Faraday Society*, *40*, 546–551. https://doi.org/10.1039/TF9444000546

Charlet, L., Alt-Epping, P., Wersin, P., & Gilbert, B. (2017). Diffusive transport and reaction inclay rocks: A storage (nuclear waste, CO2, H2), energy (shale

gas) and water quality issue [Tribute to Professor Garrison Sposito: An Exceptional Hydrologist and Geochemist]. *Advances in Water Resources*, *106*, 39–59. https://doi.org/10.1016/j.advwatres.2017.03.019

Cygan, R. T., Liang, J.-J., & Kalinichev, A. G. (2004). Molecular models of hydroxide, oxyhydroxide, and clay phases and the development of a general force field. *The Journal of Physical Chemistry B*, *108*(4), 1255–1266. https://doi.org/10.1021/jp0363287

Dang, L. X., & Chang, T. (1997). Molecular dynamics study of water clusters, liquid, and liquid-vapor interface of water with many-body potentials. *The Journal of Chemical Physics*, *106*(19), 8149–8159. https://doi.org/10.1063/1.473820

Daub, C. D., Cann, N. M., Bratko, D., & Luzar, A. (2018). Electrokinetic flow of an aqueous electrolyte in amorphous silica nanotubes. *Physical Chemistry Chemical Physics*, *20*, 27838–27848. https://doi.org/10.1039/C8CP03791D

Dazas, B., Lanson, B., Breu, J., Robert, J.-L., Pelletier, M., & Ferrage, E. (2013). Smectite fluorination and its impact on interlayer water content and structure: A way to fine tune the hydrophilicity of clay surfaces? *Microporous and Mesoporous Materials*, *181*, 233–247. https://doi.org/10.1016/j.micromeso.2013.07.032

Douillard, J., Zajac, J., Malandrini, H., & Clauss, F. (2002). Contact angle and film pressure: Study of a talc surface. *The Journal of Colloid and Interface Science*, *255*(2), 341–351. https://doi.org/10.1006/jcis.2002.8611

Du, H., & Miller, J. (2007). A molecular dynamics simulation study of water structure and adsorption states at talc surfaces. *The International Journal of Mineral Processing*, *84*(1), 172–184. https://doi.org/10.1016/j.minpro.2006.09.008

Evans, R., & Stewart, M. C. (2015). The local compressibility of liquids near non-adsorbing substrates: A useful measure of solvophobicity and hydrophobicity? *The Journal of Physics: Condensed Matter*, *27*(19), 194111. https://doi.org/10.1088/0953-8984/27/19/194111

Ferrage, E. (2016). Investigation of the interlayer organization of water and ions in smectite from the combined use of diffraction experiments and molecular simulations. A review of methodology, applications, and perspectives. *Clays and Clay Minerals*, *64*(4), 348–373. https://doi.org/10.1346/CCMN.2016.0640401

Ferrage, E., Sakharov, B., Michot, L., Delville, A., Bauer, A., Lanson, B., Grangeon, S., Frapper, G., Jimenez-Ruiz, M., & Cuello, G. (2011). Hydration properties and interlayer organization of water and ions in synthetic Na-smectite with tetrahedral layer charge. part 2. toward a precise coupling between molecular simulations and diffraction data. *The Journal of Physical Chemistry C*, *115*(5), 1867–1881. https://doi.org/10.1021/jp105128r

Ferrage, E., Seine, G., Gaillot, A., Petit, S., De Parseval, P., Boudet, A., Lanson, B., Ferret, J., & Martin, F. (2006). Structure of the 001 talc surface as seen by atomic force microscopy: comparison with X-ray and electron diffraction results. *The European Journal of Mineralogy*, *18*(4), 483–491. https://doi.org/10.1127/0935-1221/2006/0018-0483

Gao, P., Zhang, Y., Liu, X., & Lu, X. (2024). Mechanistic understanding of dehydroxylation reaction of smectites: Insights from reactive force field (reaxff) molecular dynamics simulation. *American Mineralogist*. https://doi.org/10.2138/am-2024-9445

Giese, R. F., Costanzo, P. M., & Van Oss, C. J. (1991). The surface free energies of talc and pyrophyllite. *Physics and Chemistry of Minerals*, *17*, 611–616. https://doi.org/10.1007/BF00203840

Gimmi, T., & Churakov, S. (2019). Water retention and diffusion in unsaturated clays: Connecting atomistic and pore scale simulations. *Applied Clay Science*, *175*, 169–183. https://doi.org/10.1016/j.clay.2019.03.035

Godawat, R., Jamadagni, S. N., & Garde, S. (2009). Characterizing hydrophobicity of interfaces by using cavity formation, solute binding, and water correlations. *Proceedings of the National Academy of Sciences*, *106*(36), 15119–15124. https://doi.org/10.1073/pnas.0902778106

Hånde, R., Ramothe, V., Tesson, S., Dazas, B., Ferrage, E., Lanson, B., Salanne, M., Rotenberg,B., & Marry, V. (2018). Classical polarizable force field to study hydrated hectorite: *Optimization on DFT calculations and validation against WRD data*.Minerals, *8*(5). https://doi.org/10.3390/min8050205

Heinz, H., Koerner, H., Anderson, K., Vaia, R., & Farmer, B. L. (2005). Force field for mica-type silicates and dynamics of octadecylammonium chains grafted to montmorillonite. *Chemistry of Materials*, *17*(23), 5658–5669. https://doi.org/10.1021/cm0509328

Hendricks, S. B., Nelson, R. A., & Alexander, L. T. (1940). Hydration mechanism of the clay mineral montmorillonite saturated with various cations. *The Journal of the American Chemical Society*, *62*(6), 1457–1464. https://doi.org/10.1021/ja01863a037

Jamadagni, S. N., Godawat, R., & Garde, S. (2011). Hydrophobicity of proteins and interfaces: Insights from density fluctuations. *Annual Review of Chemical and Biomolecular Engineering*, *2*, 147–171. https://doi.org/10.1146/annurev-chembioeng-061010-114156

Kaggwa, G. B., Huynh, L., Ralston, J., & Bremmell, K. (2006). The influence of polymer structure and morphology on talc wettability. *Langmuir*, *22*(7), 3221–3227. https://doi.org/10.1021/la052303i

Kamath, G., Deshmukh, S. A., & Sankaranarayanan, S. K. R. S. (2013). Comparison of select polarizable and non-polarizable water models in predicting solvation dynamics of water confined between MgO slabs. *The Journal of Physics: Condensed Matter*, *25*(30), 305003. https://doi.org/10.1088/0953-8984/25/30/305003

Koishi, A., Lee, S. S., Fenter, P., Fernandez-Martinez, A., & Bourg, I. C. (2022). Water adsorption on mica surfaces with hydrophilicity tuned by counterion types (Na, K, and Cs) and structural fluorination. *The Journal of Physical Chemistry C*, *126*(38), 16447–16460. https://doi.org/10.1021/acs.jpcc.2c04751

Landais, P. (2006). Advances in geochemical research for the underground disposal of high-level, long-lived radioactive waste in a clay formation [Extended Abstracts presented at the 7th Symp. *on the Geochemistry of the EarthÕs Surface (GES-7)]*.The Journal of Geochemical Exploration, *88*(1), 32–36. https://doi.org/10.1016/j.gexplo.2005.08.011

Le Crom, S., Tournassat, C., Robinet, J., & Marry, V. (2020). Influence of polarizability on the prediction of the electrical double layer structure in a clay mesopore: A molecular dynamics study. *The Journal of Physical Chemistry C*, *124*(11), 6221–6232. https://doi.org/10.1021/acs.jpcc.0c00190

Leroy, F., Liu, S., & Zhang, J. (2015). Parametrizing non bonded interactions from wetting experiments via the work of adhesion: *Example of water on graphene surfaces.*The Journal of Physical Chemistry C, *119*(51), 28470–28481. https://doi.org/10.1021/acs.jpcc.5b10267

Liimatainen, H., Ezekiel, N., Sliz, R., Ohenoja, K., Sirviš, J. A., Berglund, L., Hormi, O., & Ni-inimŠki, J. (2013). High-strength nanocellulose - talc hybrid barrier films. *ACS Applied Materials & Interfaces*, *5*(24), 13412–13418. https://doi.org/10.1021/am4043273

Maibaum, L., & Chandler, D. (2007). Segue between favorable and unfavorable solvation. *The Journal of Physical Chemistry B*, *111*(30), 9025–9030. https://doi.org/10.1021/jp072266z

Malikova, N., Cadone, A., Dubois, E., Marry, V., Durand-Vidal, S., Turq, P., Breu, J., Longeville, S., & Zanotti, J.-M. (2007). Water diffusion in a synthetic hectorite clay studied by quasi-elastic neutron scattering. *The Journal of Physical Chemistry C*, *111*(47), 17603– 17611. https://doi.org/10.1021/jp0748009

Marin-Laflèche, A., Haefele, M., Scalfi, L., Coretti, A., Dufils, T., Jeanmairet, G., Reed, S. K.,Serva, A., Berthin, R., Bacon, C., Bonella, S., Rotenberg, B., Madden, P. A., & Salanne, M. (2020). Metalwalls: A classical molecular dynamics software dedicated to the simulation of electrochemical systems. *The Journal of Open Source Software*, *5*(53), 2373. https://doi.org/10.21105/joss.02373

Marry, V., Dubois, E., Malikova, N., Breu, J., & Haussler, W. (2013). Anisotropy of water dynamics in clays: Insights from molecular simulations for experimental QENS analysis. *The Journal of Physical Chemistry C*, *117*(29), 15106–15115. https://doi.org/10.1021/jp403501h

Marry, V., Dubois, E., Malikova, N., Durand-Vidal, S., Longeville, S., & Breu, J. (2011). Waterdynamics in hectorite clays: Infuence of temperature studied by coupling neutron spin echo and molecular dynamics. *Environmental Science & Technology*, *45*(7), 2850–2855. https://doi.org/10.1021/es1031932

Marry, V., Le Crom, S., Ferrage, E., Michot, L., Farago, B., Delville, A., & Dubois, E. (2024). Role of cationic organization on water dynamics in saponite clays. *The Journal of Physical Chemistry C*, *128*(10), 4233–4244. https://doi.org/10.1021/acs.jpcc.3c05150

Marry, V., Malikova, N., Cadone, A., Dubois, E., Durand-Vidal, S., Turq, P., Breu, J., Longeville,S., & Zanotti, J.-M. (2008). Water diffusion in a synthetic hectorite by neutron scattering- beyond the isotropic translational model. *The Journal of Physics: Condensed Matter*, *20*(10), 104205. https://doi.org/10.1088/0953-8984/20/10/104205

https://doi.org/10.1017/cmn.2025.8 Published online by Cambridge University Press

Martin, F., Micoud, P., Delmotte, L., Marichal, C., Dred, R., Parseval, P., Mari, A., Fortune, J.-P., Salvi, S., Beziat, D., Grauby, O., & Ferret, J. (1999). The structural formula of talc from the Trimouns deposit, Pyrenees, france. *Canadian Mineralogist*, *37*, 997–1006.

Mering, J. (1946). On the hydration of montmorillonite. *Transactions of the Faraday Society*, *42*, B205–B219. https://doi.org/10.1039/TF946420B205

Michot, L. J., Villieras, F., Francois, M., Yvon, J., Le Dred, R., & Cases, J. M. (1994). The structural microscopic hydrophilicity of talc. *Langmuir*, *10*(10), 3765–3773. https://doi.org/10.1021/la00022a061

Monroe, J., Barry, M., De Stefano, A., Aydogan Gokturk, P., Jiao, S., Robinson-Brown, D., Webber, T., Crumlin, E. J., Han, S., & Shell, M. S. (2020). Water structure and properties at hydrophilic and hydrophobic surfaces. *Annual Review of Chemical and Biomolecular Engineering*, *11*, 523–557. https://doi.org/10.1146/annurev-chembioeng-120919-114657

Nalaskowski, J., Abdul, B., Du, H., & Miller, J. (2007). Anisotropic character of talc surfaces as revealed by streaming potential measurements, atomic force microscopy, molecular dynamics simulations and contact angle measurements. *Canadian Metallurgical Quarterly*, *46*(3), 227–235. https://doi.org/10.1179/cmq.2007.46.3.227

Pitman, M., & van Duin, A. T. (2012). Dynamics of confined reactive water in smectite clay-zeolite composites. *The Journal of the Americal Chemical Society*, *134*(6), 3042–3053. https://doi.org/10.1021/ja208894m

Plimpton, S. (1995). Fast parallel algorithms for short-range molecular dynamics. *The Journal of computational physics*, *117*(1), 1–19.

Ravipati, S., Aymard, B., Kalliadasis, S., & Galindo, A. (2018). On the equilibrium contact angle of sessile liquid drops from molecular dynamics simulations. *The Journal of Chemical Physics*, *148*(16), 164704.

Rotenberg, B., Patel, A. J., & Chandler, D. (2011). Molecular explanation for why talc surfaces can be both hydrophilic and hydrophobic. *The Journal of the American Chemical Society*, *133*(50), 20521–20527. https://doi.org/10.1021/ja208687a

Sato, T., Watanabe, T., & Otsuka, R. (1992). Effects of layer charge, charge location, and energy change on expansion properties of dioctahedral smectites. *Clays and Clay Minerals*, *40*, 103–113. https://doi.org/10.1346/CCMN.1992.0400111

Skipper, N. T., Refson, K., & McConnell, J. D. C. (1989). Computer calculation of water-clay interactions using atomic pair potentials. *Clay Minerals*, *24*(2), 411–25. https://www.cambridge.org/core/journals/clay-minerals/article/abs/computer-calculation-of-waterclay-interactions-using-atomic-pair-potentials/0CF5AD11B100771F586E2DDE3A09727E

Surblys, D., Leroy, F., Yamaguchi, Y., & Müller-Plathe, F. (2018). Molecular dynamics analysis of the influence of Coulomb and van der Waals interactions on the work of adhesion at the solid-liquid interface. *The Journal of Chemical Physics*, *148*(13), 134707. https://doi.org/10.1063/1.5019185

Szczerba, M., Kalinichev, A. G., & Kowalik, M. (2020). Intrinsic hydrophobicity of smectite basal surfaces quantitatively probed by molecular dynamics simulations. *Applied Clay Science*, *188*, 105497. https://doi.org/10.1016/j.clay.2020.105497

Tazi, S., Boţan, A., Salanne, M., Marry, V., Turq, P., & Rotenberg, B. (2012). Diffusion coefficient and shear viscosity of rigid water models. *The Journal of Physics: Condensed Matter*, *24*(28), 284117. https://doi.org/10.1088/0953-8984/24/28/284117

Tazi, S., Molina, J. J., Rotenberg, B., Turq, P., Vuilleumier, R., & Salanne, M. (2012). A transferable ab initio based force field for aqueous ions. *The Journal of Chemical Physics*, *136*(11). https://doi.org/10.1063/1.3692965

Teleman, O., Jšnsson, B., & Engstršm, S. (1987). A molecular dynamics simulation of a water model with intramolecular degrees of freedom. *Molecular Physics*, *60*(1), 193–203. https://doi.org/10.1080/00268978700100141

Tesson, S., Louisfrema, W., Salanne, M., Boutin, A., Ferrage, E., Rotenberg, B., & Marry, V.(2018). Classical polarizable force field to study hydrated charged clays and zeolites. *The Journal of Physical Chemistry C*, *122*(43), 24690–24704. https://doi.org/10.1021/acs.jpcc.8b06230

Tesson, S., Louisfrema, W., Salanne, M., Boutin, A., Rotenberg, B., & Marry, V. (2017). Classical polarizable force field to study dry charged clays and zeolites. *The Journal of Physical Chemistry C*, *121*(18), 9833–9846. https://doi.org/10.1021/acs.jpcc.7b00270

Tesson, S., Salanne, M., Rotenberg, B., Tazi, S., & Marry, V. (2016). Classical polarizable forcefield for clays: Pyrophyllite and talc. *The Journal of Physical Chemistry C*, *120*(7), 3749–3758. https://doi.org/10.1021/acs.jpcc.5b10181

Wang, J., Savoye, S., Ferrage, E., Hubert, F., Lefevre, S., Radwan, J., Robinet, J., Tertre, E., & Gouze, P. (2022). Water and ion diffusion in partially water saturated compacted kaolinite: Role played by vapor-phase diffusion in water mobility. *The Journal of Contaminant Hydrology*, *248*, 103989. https://doi.org/10.1016/j.jconhyd.2022.103989

Washburn, E. (1921). The dynamics of capillary flow. *Physical Review*, *17*, 273. https://doi.org/10.1103/PhysRev.17.273

Wenzel, R. N. (1936). Resistance of solid surfaces to wetting by water. *Industrial & Engineering Chemistry*, *28*(8), 988–994. https://doi.org/10.1021/ie50320a024

Wick, C., & Cummings, O. (2011). Understanding the factors that contribute to ion interfacial behavior. *Chemical Physics Letters*, *513*, 161–166. https://doi.org/10.1016/j.cplett.2011.06.052

Wilding, N. B., Evans, R., & Turci, F. (2024). What is the best simulation approach for measuring local density fluctuations near solvo-/hydrophobes? *The Journal of Chemical Physics*, *160*(16), 164103. https://doi.org/10.1063/5.0203088

Willard, A. P., & Chandler, D. (2014). The molecular structure of the interface between water and a hydrophobic substrate is liquid-vapor like. *The Journal of Chemical Physics*, *141*(18), 18C519. https://doi.org/10.1063/1.4897249

Yang, X., An, C., Feng, Q., Boufadel, M., & Ji, W. (2022). Aggregation of microplastics and clay particles in the nearshore environment: Characteristics, influencing factors, and implications. *Water Research*, *224*, 119077. https://doi.org/10.1016/j.watres.2022.119077

Yang, Y., Churakov, S., Patel, R., Prasianakis, N., Deissmann, G., Bosbach, D., & Poonoosamy,J. (2024). Pore-scale modeling of water and ion diffusion in partially saturated clays. *Water Resources Research*, *60*(1). https://doi.org/10.1029/2023WR035595

Ye, X., Cheng, Z., Wu, M., Hao, Y., Lu, G., Hu, X. B., Mo, C., Li, Q., Wu, J., & Wu, J. (2022). Effects of clay minerals on the transport of polystyrene nanoplastic in groundwater. *Water Research*, *223*, 118978. https://doi.org/10.1016/j.watres.2022.118978

Yin, X., & Miller, J. (2012). Wettability of kaolinite basal planes based on surface force measurements using atomic force microscopy. *Mining, Metallurgy & Exploration*, *29*, 13–19.

Young, T. (1805). An essay on the cohesion of fluids. *Philosophical Transactions*, *95*, 65. https://doi.org/10.1098/rstl.1805.0005

Yuan, D., Xie, L., Shi, X., Yi, L., Zhang, G., Zhang, H., Liu, Q., & Zeng, H. (2018). Selective flotation separation of molybdenite and talc by humic substances. *Minerals Engineering*, *117*, 34–41. https://doi.org/10.1016/j.mineng.2017.12.005

Yuet, P. K., & Blankschtein, D. (2010). Molecular dynamics simulation study of water surfaces: Comparison of flexible water models. *The Journal of Physical Chemistry B*, *114*(43), 13786–13795. https://doi.org/10.1021/jp1067022

Zhang, Y., Liu, X., van Duin, A. C. T., Lu, X., & Meijer, E. (2024). Development and validation of a general-purpose reaxff reactive force field for earth material modeling. *The Journal of Chemical Physics*, *160*(9), 094103. https://doi.org/10.1063/5.0194486

https://doi.org/10.1017/cmn.2025.8 Published online by Cambridge University Press